Biomaterials 35 (2014) 4678–4687

Contents lists available at ScienceDirect

Biomaterials

journal homepage: www.elsevier.com/locate/biomaterials

Dual functional AuNRs@MnMEIOs nanoclusters for magnetic resonance imaging and photothermal therapy

Yao-Chen Chuang [a], Chia-Jung Lin [a,1], Shih-Feng Lo [a], Jei-Lin Wang [a], Shey-Cherng Tzou [a], Shyng-Shiou Yuan [b,**], Yun-Ming Wang [a,c,*]

[a] Department of Biological Science and Technology, Institute of Molecular Medicine and Bioengineering, National Chiao Tung University, 75 Bo-Ai Street, Hsinchu 30068, Taiwan
[b] Translational Research Center, Cancer Center, and Department of Obstetrics and Gynecology, Kaohsiung Medical University, Kaohsiung 80708, Taiwan
[c] Department of Biomedical Science and Environmental Biology, Kaohsiung Medical University, Kaohsiung 80708, Taiwan

ARTICLE INFO

Article history:
Received 24 January 2014
Accepted 12 February 2014
Available online 7 March 2014

Keywords:
MR imaging
Gold nanorods
Manganese-doped iron oxide
Theranosis
Photothermal

ABSTRACT

A novel dual functional theranosis platform is developed based on manganese magnetism-engineered iron oxide (MnMEIO) and gold nanorods (AuNRs) to combine magnetic resonance (MR) imaging and photothermal therapy in one nanocluster. The platform showed improved T_2-*weighted* MR imaging and exhibited a near-infrared (NIR) induced temperature elevation due to the unique characteristics of AuNRs@MnMEIOs nanoclusters. The obtained dual functional spherical-shaped nanoclusters showed low cytotoxicity, and high cellular uptake efficiency. The AuNRs@MnMEIOs nanoclusters also demonstrated a 1.9 and 2.2 folds r_2 relaxivity value higher than those of monodispersed MnMEIO and Resovist. In addition, *in vivo* MR imaging study found that the contrast enhancements were $-70.4 \pm 4.3\%$ versus $-7.5 \pm 3.0\%$ in Her-2/neu overexpression tumors as compared to the control tumors. More importantly, NIR laser irradiation to the tumor site resulted in outstanding photothermal therapeutic efficacy and without damage to the surrounding tissue. In additional, the prepared dual functional AuNRs@MnMEIOs display high stability and furthermore disperse even in the presence of external magnet, showing that AuNRs@MnMEIOs nanoclusters can be manipulated by an external magnetic field. Therefore, such nanoclusters combined MR imaging and photothermal therapeutic functionality can be developed as a promising nanosystem for effective cancer diagnosis and therapy.

1. Introduction

Recently, nanostructured materials have received great attention in biomedical imaging, diagnosis, and therapy [1,2]. Each of these methods possesses characteristic strengths and weaknesses, but none of them are capable of independently providing complete structural and functional information. The accuracy of tumor detection can be greatly improved by integrating the different individual imaging modalities. Therefore, various types of hybrid nanoparticles that have been used for multimodal imaging, based on the incorporation of several contrast agents into one single system, will enable the development of multifunctional nanomedical platforms for multimodal imaging [3,4]. Moreover, these hybrid platforms could simultaneous diagnose and treat patients by combining therapeutic and diagnostic capabilities into one single agent. Thus the hybrid systems provide more specific and efficient ways for the treating diseases than single-modality nanoparticle [5]. Among various nanomaterials, gold and superparamagnetic iron oxide (SPIO) nanoparticles are highly promising for the development of "theranosis" agents [6–9]. Combining iron oxide and gold in one multifunctional agent could enhance diagnosis and therapeutic heating in the targeting tumors due to excellent magnetic properties (from iron oxide), and optical (from gold). Over the past few years, many research efforts have been focused on developing such dual functional nanomaterials including heterodimer nanocompositions [10,11] and core–shell nanostructure [12–15]. Among various forms of particle geometries, gold nanomaterials, especially gold nanorods (AuNRs) can be adjusted by tuning their morphology to exhibit distinctive optical properties in near-infrared (NIR) region (700–850 nm). Due to

* Corresponding author. Department of Biological Science and Technology, Institute of Molecular Medicine and Bioengineering, National Chiao Tung University, 75 Bo-Ai Street, Hsinchu 30068, Taiwan. Tel.: +886 3 5729287; fax: +886 3 5729288.
** Corresponding author.
E-mail address: ymwang@mail.nctu.edu.tw (Y.-M. Wang).
[1] Author for equal contribution for first author.

http://dx.doi.org/10.1016/j.biomaterials.2014.02.026
0142-9612/

minimal attenuation by water and hemoglobin at these wavelengths, which absorb weakly in soft tissue and blood, AuNRs is particularly interesting for the development of NIR absorption photothermal therapy [16–18]. Hence, a nanostructure that combines MR image diagnosis and NIR photothermal ablation would greatly increase the treatment efficacy and simultaneously minimize the damage to normal cells and tissues. However, the gold coating on iron oxide nanoparticles display intense NIR absorbance is difficult to synthesize; [19–21] On the other hand, controlling the hydrodynamic size of nanocompositions between 10 nm and 100 nm to avoid elimination by reticuloendothelial system (RES) is also a major challenge to design ideal platforms [22,23].

Herein, we described a novel strategy of dual functional nanoclusters based on manganese-doped magnetism-engineered iron oxide (MnMEIO) and AuNRs which combined with optical and magnetic properties useful in MR imaging and photothermal ablation functions. The size of the dual functional nanocluster was controlled below 100 nm to avoid elimination by clearance organs. Furthermore, we studied the effect of nanocluster shape on cellular uptake. The MnMEIO in our platform can be used as MR imaging contrast agent and the photothermal ablation function of AuNRs was also demonstrated in this work. Scheme 1 depicted the novel dual functional nanocluster. MnMEIO attracted AuNRs through a well-understood chemistry of Au–S bond [24]. Then AuNRs and MnMEIOs nanoclusters (abbreviated as AuNRs@MnMEIOs) were further stabilized with acryl-modified poly(ethylene glycol) (PEG-Ac) and conjugated with Herceptin for targeting to Her-2/neu human breast cancer cells (SKBR-3). *In vitro* and *in vivo* efficacies of the AuNRs@MnMEIOs-Herceptin for theranosis were evaluated through confocal fluorescent microscopic studies, MR imaging, optical imaging and photothermal therapy studies.

2. Experimental section

2.1. Chemicals and materials

Osmium tetroxide (1%), iron (III) acetylacetonate ($Fe(acac)_3$, 99.9%), manganese (II) acetylacetonate ($Mn(acac)_2$, 99%), oleic acid (90%), oleylamine (90%), 1,2-hexadecandiol (90%), benzyl ether (≥98%), poly(ethylene glycol) methyl ether (mPEG, average $M_w \cong 2000$), N-ethyl-N′-(3-dimethylaminopropyl) carbodiimide (EDC), fluorescein isothiocyanate (FITC), sodium cacodylate trihydrate (≥98%), tannic acid (99%), and glutaraldehyde (25%) were purchased from Sigma Aldrich (MO, USA). Acetyl chloride (96%), cetyl trimethylammonium bromide (CTAB) (98%), and (3-mercaptopropyl) trimethoxysilane (MPTES, 95%) were purchased from Alfa Aesar (MA, USA). (3-Aminopropyl) triethoxy silane (APTES, 98%) and N′-hydroxysuccinimide (NHS, 97%) were purchased from Fluka (Buchs, Switzerland). Herceptin (Trastumab) was purchased from Roche (Basel, Switzerland). Molecular-porous membrane tubings (average $M_w \cong 12–14$ kDa and average $M_w \cong 300$ kDa) were purchased from Spectrum (TX, USA). 3-(4, 5-Dimethyl-2-thiazolyl)-2, 5-diphenyl-2H-tetrazolium bromide and thiazole Blue were purchased from Merck (Dietikon, Switzerland). S162 Scientific Formvar/Carbon200-mesh copper (50-grid) was purchased from Agar Scientific (Stansted, UK). Matrigel was purchased from BD Bioscience (MA, USA). Spurr's resin was purchased from Agar Scientific (Essex, UK). All solvents were purchased from Echo Chemical (Miaoli, Taiwan). Dulbecco's minimal essential medium (DMEM), fetal bovine serum (FBS), penicillin, and streptomycin were purchased from Gibco (NY, USA).

2.2. Cell line and tumor model

SKBR-3, a human breast cancer cell line, and Colo-205, a human colorectal cancer cell line, were obtained from Food Industry Research and Development Institute (FIRDI, Hsinchu, Taiwan). Cells were cultured in DMEM and supplemented with 10% FBS, 100 U mL^{-1} penicillin and 100 μg mL^{-1} streptomycin at 37 °C in an atmosphere of 5% CO_2. Nu mice (4 weeks old) were obtained from the BioLASCO (Yi-Lan, Taiwan). Animal experiments were performed in accordance with institute guidelines.

2.3. Characterization

Relaxation time values (T_1 and T_2) of MnMEIO samples were measured to determine relaxivity r_1 and r_2. All measurements were made using the relaxometers (NMS-120 & MQ60 Minispec, Bruker, Ontario, Canada) operating at 20 and 60 MHz and 37.0 ± 0.1 °C. Hydrodynamic size and zeta potential were analyzed by Zetasizer (Nano ZS90, Malvern Instruments, UK). The compositions of AuNRs@MnMEIOs-PEG were obtained by an Energy-dispersive X-ray spectrometer (EDX, S-3000N, Hitachi, Tokyo, Japan) and inductively coupled plasma atomic emission spectroscopy (ICP-AES, Jobin-Yvon JY 38type III, Edison, New Jersey, USA). Magnetic properties of the MnMEIO-PEG and AuNRs@MnMEIOs-PEG were studied with superconducting quantum interference devise magnetometer (SQUID, VSM Model 7400, OH, USA) at fields ranging from −10 to 10 kOe and at 300 K. The average core size, size distribution, and morphology were examined using a transmission electron microscope (TEM, JEOL JEM-2000 EX II, Tokyo, Japan) at a voltage of 80 kV. The composite dispersion was drop-cast onto a 200-mesh copper grid and the grid was air-dried at room temperature before being loaded into the microscope.

2.3.1. Synthesis of methoxy poly(ethylene glycol) acrylate (mPEG-Ac)

Poly(ethylene glycol) methyl ether (mPEG, 40 g, 20 mmol) was dispersed in 200 mL of anhydrous dichloromethane (DCM) in a 250 mL round-bottom flask and cooled to 0 °C using an ice-bath with stirring. Then, acetyl chloride (2.4 mL,

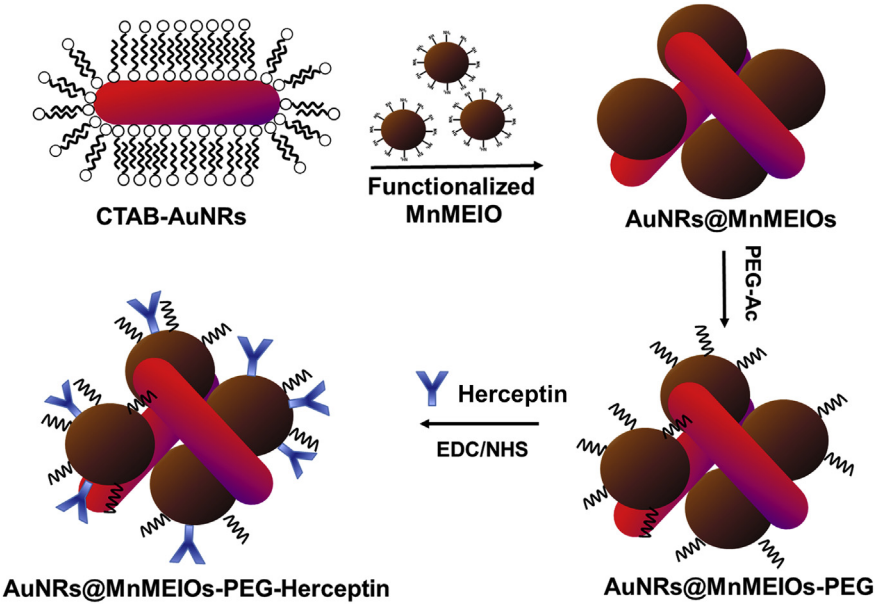

Scheme 1. Schematic illustration showed that AuNRs@MnMEIOs nanoclusters were prepared. The AuNRs@MnMEIOs nanoclusters were used as a T_2 constrast agent and photo-induced heating agent.

30 mmol) and triethanolamine (TEA) (4.2 mL, 30 mmol) were added and the mixture was stirred at room temperature for 48 h under nitrogen atmosphere. The reaction mixture was filtered using a filter funnel and the solvent was evaporated to obtain the crude product, which was further precipitated in hexane. The final product was dried under vacuum for overnight. 1H NMR (300 MHz, $CDCl_3$) d (ppm): 3.37 (s, 3H, CH_3–O), 3.63 (m, 104H, PEG chain protons), 4.30 (t, J = 4.7 Hz, 2H, C–CH_2–C=O), acryl group: 5.56 (1H), 6.15 (1H), 6.37 (1H).

2.3.2. Synthesis of functionalized magnetic nanoparticles

MnMEIOs capped with oleic acid was synthesized by thermal decomposition under nitrogen atmosphere [25]. Briefly, $Fe(acac)_3$ (1.4 g, 4 mmol), $Mn(acac)_2$ (0.51 g, 2 mmol), 1,2-hexadecanediol (2.58 g, 10 mmol), oleic acid (1.7 g, 6 mmol), oleylamine (1.6 g, mmol), and benzyl ether (5 mL) were mixed and stirred under nitrogen atmosphere. The mixture was heated to 200 °C and maintained to reflux for 2 h. Then, it was heated to 300 °C and refluxed for 1 h. The reaction mixture was cooled to room temperature. Then, the black solution was precipitated with acetone and separated via centrifugation. After discarding the supernatant, the black product was dissolved in hexane. Centrifugation (3000 rpm, 10 min) was applied to remove the undispersed residue. The product, MnMEIOs, was then precipitated with acetone, centrifuged to remove the solvent, and redispersed into chloroform. The surface of the MnMEIOs was functionalized with organosilane molecules (APTES and MPTES) to generate an amine and thiol terminated surface [26]. APTES and MPTMS functionalization was performed by silane ligand exchange. Briefly, 0.5% (v/v) APTES and 0.25% (v/v) MPTES were added to the MnMEIOs in toluene containing 0.01% (v/v) acetic acid causing precipitation of the particles. The mixture was sonicated for 6 h and then rinsed and redispersed with water to remove excess APTES and MPTES.

2.3.3. Synthesis of gold nanorods (AuNRs)

Gold nanorods were modified and synthesized using the previous procedures [27,28]. Briefly, the formation of short AuNRs was produced by the addition 3.2 mL of 5 mM HAuCl4 and 72 μL HCl (37 wt. % in water, 12.1 M) to 15 mL of 0.2 mM CTAB aqueous solution and stirred for 15 min at 700 rpm. The solution was then mixed with 2.56 mL of 10 mM ascorbic acid and 16 μL of 100 mM $AgNO_3$. Next, 40 μL of 10 mM $NaBH_4$ was finally added to the mixture to initiate growth to yield gold nanorods of aspect ratio about 3. The formation of short nanorods was visually observed by the formation of a red-colored solution within 30 min. Complete short AuNRs was monitored by solution extinction measurements. Finally, excess CTAB was removed by centrifuging twice at 10,000 rpm, the supernatant was remove the solvent, and redispersed into deionized water.

The long AuNRs were synthesized using the binary surfactant. Briefly, the seed solution for AuNRs growth was prepared as follows: 5 mL of 0.5 mM $HAuCl_4$ was mixed with 5 mL of 0.2 M CTAB solution, then, 600 μL of fresh 10 mM $NaBH_4$ was injected to the Au(III)-CTAB solution under vigorous stirring at 1,200 rpm. The seed solution was aged at room temperature for 30 min before use. The growth solution containing 0.137 g of CTAB and 0.025 g of sodium oleate in 5 mL of deionized water was reacted at 30 °C and mixed with 19.2 μL of 100 mM $AgNO_3$ solution. Then which 5 mL of 1 mM $HAuCl_4$ solution was added and stirred for 90 min and 72 μL of HCl (37 wt. % in water, 12.1 M) was added to adjust the pH. After another 15 min of slow stirring at 400 rpm, 1.25 mL of 64 mM ascorbic acid was added and the solution was vigorously stirred for 30 s. Finally, 16 μL of seed solution was injected into the growth solution. The resultant mixture was stirred for 30 s and left undisturbed at 30 °C for 12 h for AuNR growth. The final products were isolated by centrifugation at 7,000 rpm for 30 min followed by removal of the supernatant.

2.3.4. Preparation of spherical-shaped and rod-shaped AuNRs@MnMEIOs-PEG-Herceptin

Using the reported extinction coefficients of the longitudinal plasmon peaks [29], the molar concentration in nanoparticles of all AuNR solutions were prepared before used. To establish spherical-shaped AuNRs@MnMEIOs, 2 mL of functionalized-MnMEIOs was added into 4 mL of 10 nM CTAB-AuNRs solution (both short aspect ratio and long aspect ratio AuNRs) and shaken for 12 h at room temperature. Then, 300 μL of 2% mPEG-Ac was added to the mixture and stirred for 3 h at room temperature. The spherical-shaped AuNRs@MnMEIOs-PEG was obtained and purified by dialysis to remove excess mPEG-Ac and CTAB. To establish rod-shaped AuNRs@MnMEIOs, the process was similar with spherical-shaped AuNRs@MnMEIOs, after removing excess mPEG-Ac and CTAB, 300 μL of 2% NH_2-PEG_{3500}-SH was added to the mixture and stirred for 3 h at room temperature to modify the surface AuNRs, the rod-shaped AuNRs@MnMEIOs-PEG was obtained and purified by dialysis to remove excess NH_2-PEG_{3500}-SH. To prepare dual functionalization nanocompositions, AuNRs@MnMEIOs-PEG-Herceptin, three hundreds microliters of 1.6 mg mL^{-1} EDC and 1 mg mL^{-1} NHS were added into both spherical-shaped and rod-shaped AuNRs@MnMEIOs-PEG solution. Then, 2 μL of 22 mg mL^{-1} Herceptin was added into the mixture and incubated for 90 min at room temperature. The Herceptin-modified AuNRs@MnMEIOs-PEG was isolated by centrifugation at 8,000 rpm for 30 min at 4 °C to remove the excess EDC, NHS, Herceptin and unbound MnMEIOs (i.e. spherical-shaped AuNRs@MnMEIOs-PEG-Herceptin and rod-shaped AuNRs@MnMEIOs-PEG-Herceptin, respectively). The final products were kept at 4 °C in PBS before used.

2.4. Evaluation of intracellular distribution of AuNRs@MnMEIOs nanoclusters

Human breast cancer cell line (SKBR-3) (1×10^6 cells) were seeded onto round glass coverslips placed in 6-well plates and cultured overnight. After cells attached, cells were incubated with 1 mM (based on Fe and Mn concentration) of AuNRs@MnMEIOs-FITC-PEG-Herceptin for 24 h at 37 °C. At the end of the incubation period, the cells were washed with PBS for 2 times to remove any free AuNRs@MnMEIOs-FITC-PEG-Herceptin and then fixed with 4% formaldehyde solution at room temperature for 30 min. Coverslips were placed onto glass microscope slides, and the distribution of AuNRs@MnMEIOs-FITC-PEG-Herceptin was analyzed using a confocal laser scanning (CLS) imaging system (TCS-SP5-X AOBS, Leica, Germany) consisting of Olympus BX51 microscope (Olympus, Tokyo, Japan) and a 20 mW-output 488 nm argon ion laser.

2.5. Cell viability determination

SKBR-3 cells were seeded in a 24-well plate at a density of 1×10^5 cells per well and were allowed to attach for 24 h at 37 °C in a 5% CO_2 incubator before the treatment. Cells were maintained at 37 °C for 24 h after treatment with CTAB-AuNRs or AuNRs@MnMEIOs-PEG-Herceptin at different concentrations (625 pM–2 nM based on AuNRs). Cell viability was then determined using the MTT (3-(4, 5-Dimethylthiazol-2-yl)-2, 5-diphenyl tetrazolium bromide) assay. Viable cells are capable of metabolizing the MTT reagent while dead cells are not. The treated cells were incubated with the MTT reagent for 4 h. Then 500 μL DMSO was added to each well and incubated for 10 min and the absorbance at 540 nm was read. Each concentration was repeated in triplicate and the results expressed as percentages relative to the control.

2.6. Nanoclusters cellular uptake study

To compare the cellular uptake of efficiency of different morphologies of AuNRs@MnMEIOs-PEG nanoclusters (with and without Herceptin), both Prussian blue staining and TEM were used to analyze. For Prussian blue staining, SKBR-3 (approximately 1×10^6 cells) were seeded in T25 flask. After cells attached, media was replaced with medium containing spherical-shaped or rod-shaped AuNRs@MnMEIOs-PEG-Herceptin (56 μg mL^{-1}, based on the concentration of Fe and Mn). At the end of the incubation period, the cells were washed with PBS for 2 times to remove unbound AuNRs@MnMEIOs-PEG-Herceptin. Cells were fixed with 4% paraformaldehyde for 40 min. Then, cells were incubated with fresh prepared Perls' reagent (4% potassium ferrocyanide/20% HCl, 1:1, v/v) for 30 min and subsequently observed by an inverted optical microscope. The uptake efficiency of different morphologies was also monitored by TEM to further validate the cellular uptake in SKBR-3 cells. For this experiment, SKBR-3 cells (approximately 1×10^7 cells per T75 flask) were incubated with medium containing spherical-shaped or rod-shaped AuNRs@MnMEIOs-PEG-Herceptin (56 μg mL^{-1}, based on the concentration of Fe and Mn) for 4 h. Treated cells were centrifuged and fixed with paraformaldehyde (1.6%)-glutaraldehyde (2.5%) solution followed by OsO_4 solution. Then, cells were dehydrated in a graded series of ethanol and acetone and embedded in Spurr resin. These cell-containing resin blocks were sectioned using an ultramicrotome and ultrathin sections (70–90 nm thickness) were transferred onto TEM grid.

2.7. Intracellular iron content measurement

For the intracellular iron content quantification, cells were incubated with AuNRs@MnMEIOs nanocluster (56 μg mL^{-1}, based on the concentration of Fe and Mn) for 12 h. The cells were washed, collected, and counted. After 1500 *g* centrifugation for 10 min, the cell pellets were resuspended in 100 μL 12% HCl solution and incubated at 60°C for 6 h. After incubation, the suspension was centrifuged at 12,000× *g* for 10 min, and the supernatants were collected for iron concentration quantification. Fifty μL of 1% ammonium persulfate was added into 50 μL sample solution to oxidize the ferrous ions to ferric ions. Finally, 100 μL of 0.1 M potassium thiocyanate was added to the solution and incubated for 5 min to form the red color iron-thiocyanate. The absorption was read by a microplate reader set at 490 nm.

2.8. In vitro and in vivo MR imaging studies

MR imaging was performed on a 7.0 T MR imaging system (Bruker, Ettlingen, Germany). For *in vitro* MR imaging studies, SKBR-3 and Colo-205 cells (1×10^6 cells) were incubated with AuNRs@MnMEIOsnanoclusters (56 μg mL^{-1} based on the concentration of Fe and Mn) at 37 °C for 24 h and washed three times in PBS. A T_2-*weighted* spin-echo sequence (TR/TE = 3000 ms/22 ms) was used for MR imaging. For *in vivo* MR imaging studies, cultured SKBR-3 and Colo-205 tumor cells (3×10^6 cells/mouse) were injected in their right and left thigh regions to establish the tumors bearing mice model. After the tumors developed up to a size of approximately 200 mm^3, AuNRs@MnMEIOs-PEG-Herceptin (10 mg kg^{-1} body weight) were intravenous (i.v.) injected via the tail vein into the mice. The whole-body imaging of pentobarbital-anesthetized mice was performed with a 7.0 T MR imaging system. All samples were scanned by a fast gradient echo pulse sequence with the following parameters: TR/TE = 3000 ms/22 ms, matrix size = 256 × 256,

FOV = 6 × 6 mm and data are represented as mean ± SD (n = 5). The contrast enhancement (%) was calculated by the following equation (1):

$$\text{Enhancement}\ (\%) = (SI_{post} - SI_{pre})/SI_{pre} \times 100 \quad (1)$$

where SI_{post} is the value of signal intensity in tumor cells treated with the contrast agents, AuNRs@MnMEIOs-PEG-Herceptin, and SIpre is the value of signal intensity for tumor cells alone.

2.9. In vivo systematic toxicity

For *in vivo* systematic toxicity study, a total of 4 tumors bearing mice were allocated to 2 groups, a) control group (without AuNRs@MnMEIOs-PEG-Herceptin treatment, b) with AuNRs@MnMEIOs-PEG-Herceptin treatment (10 mg kg^{-1}). After AuNRs@MnMEIOs-PEG-Herceptin injection, were sacrificed by CO_2 asphyxiation. A full necropsy was performed and the organs were harvested, fixed in 10% neutral buffered formalin, embedded in paraffin, sectioned, and stained with hematoxylin and eosin for histological exaination using standard techniques. Examined tissues included: liver, spleen, lung, kidney, and heart.

2.10. Thermal response measurements

The average temperature elevation of AuNRs@MnMEIOs nanoclusters was measured by placing the AuNRs@MnMEIOs nanoclusters with different concentrations (100 μL, 0.12 nM–1 nM based on the concentration of AuNRs) in 96-well plates and irradiated using a 808 nm diode continuous wavelength (CW) laser source (Pretek, Taiwan) at a power density of 5 W cm^{-2}. A themometer (TM-924C) from Lutron (Taipei, Taiwan) fitted with a K-type thremocouple (not exposed to the laser beam) was immersed in the AuNRs@MnMEIOs solutions to record the temperature. For control experiment, same volume of water without the AuNRs@MnMEIOs solution was irradiated with CW laser and recorded its temperature.

2.11. Photothermal ablation study

Human breast cancer cell line SKBR-3 (1×10^4 cells) were seeded in 96-well plates and cultured overnight at 37 °C in a 5% CO_2 incubator before the treatment. Afterward cells were incubated with AuNRs@MnMEIOs-PEG-Herceptin nanoclusters for 6 h in the cell culture medium. Cells were irradiated at 808 nm CW laser for 10 min with power intensity of 5 Wcm^{-2}. To evaluate cell viability after irradiation, the cells were then stained with Calcein AM (BD Bioscience, CA, USA) and Propidium Iodide (PI) (Calbiochem, NJ, USA). Then, the cells were observed using a laser scanning confocal imaging system. For *in vivo* experiments, after the mice were intravenous injected with 200 μL of AuNRs@MnMEIOs-PEG-Herceptin (10 mg kg^{-1} body weight) for 24 h, the tumor on each mouse was radiated by the 808 nm NIR laser at the power density of 5 W cm^{-2} for 10 min. Four groups of mice (untreated, laser only, AuNRs@MnMEIOs-PEG-Herceptin only, and AuNRs@MnMEIOs-PEG-Herceptin + laser) with five mice per group were used as the control. The tumor sizes were measured by a caliper every four day and calculated by the following equation (2):

$$\text{Volume} = (\text{tumor length}) \times (\text{tumor width})^2/2 \quad (2)$$

Relative tumor volumes were calculated as V/V_0 (V_0 was the tumor volume when the treatment was initiated). Mice with tumor sizes exceeding 4,000 mm^3 were euthanatized according to the animal protocol.

3. Results and discussion

3.1. Characterization of AuNRs@MnMEIOs nanoclusters

The monodispersed MnMEIOs and CTAB-AuNRs were synthesized following the previously reported methods. The morphology of MnMEIOs and CTAB-AuNRs can be clearly observed in Fig. 1. Two hundred particles were counted and measured per sample. TEM images showed that the monodispersed MnMEIOs have an overall particle size of 8.2 ± 1.3 nm and the CTAB-AuNRs with average length and width 31.2 ± 2.9 and 10.6 ± 1.5 nm, respectively. Subsequently, the AuNRs@MnMEIOs nanoclusters were prepared through the conjugation of thiol-functionalized MnMEIOs with AuNRs. A near sphere nanocluster was shown in Fig. 1C, the average size of AuNRs@MnMEIOs nanoclusters is 53.2 ± 6.9 nm. The hydrodynamic size and zeta potential were determined (Table S1). The hydrodynamic size of MnMEIO and AuNRs had a relatively narrow size distribution with a mean size of 15.2 ± 2.5 nm and 28.1 ± 1.8 nm, respectively. Upon conjugation of

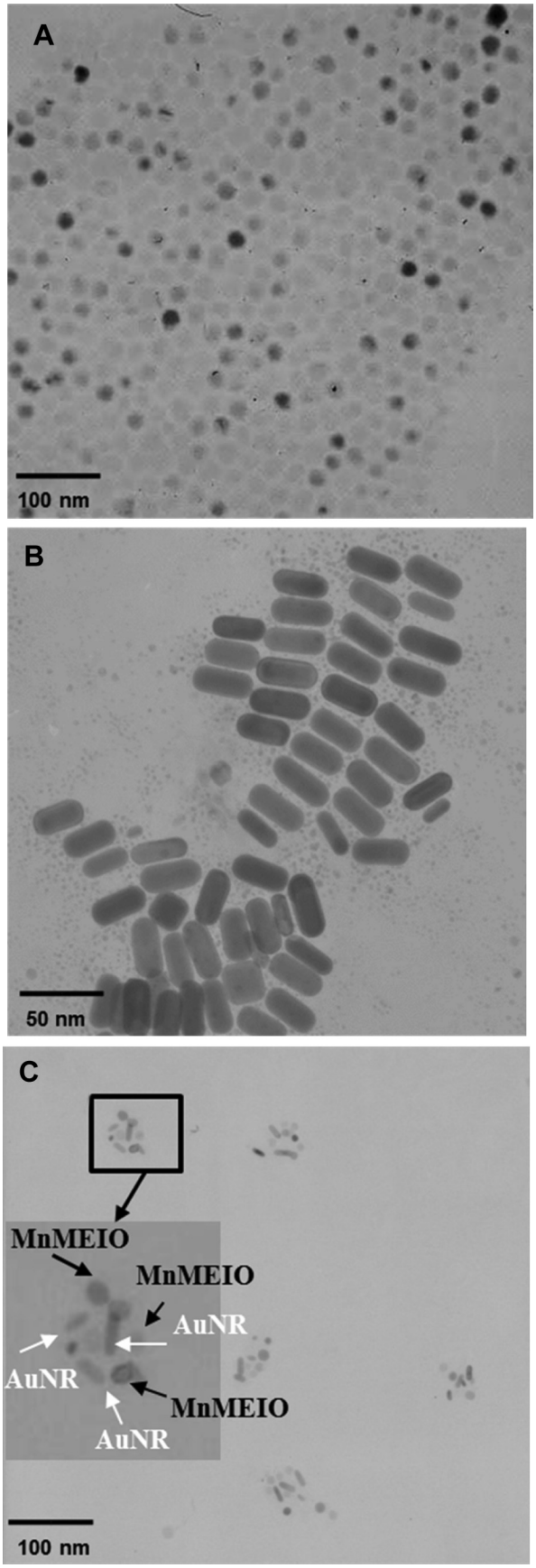

Fig. 1. TEM image of (A) MnMEIOs, (B) CTAB-AuNRs, and (C) AuNRs@MnMEIOs.

thiol-functionalized MnMEIO, CTAB-AuNRs, PEG-Ac and Herceptin antibody, the hydrodynamic size of the nanoclusters increased to 64.2 ± 6.3 nm. Furthermore, the zeta potential values of MnMEIO, CTAB-AuNRs, and AuNRs@MnMEIOs nanoclusters were found to be +29.4 ± 4.3, +46.3 ± 1.5, and −6.3 ± 0.5 mV, respectively. The decrease in zeta potential can be attributed to CTAB removal from the surface of AuNRs, and PEG masking of the surface charges [30–32]. Figure S1 showed the UV/vis spectra of MnMEIO-PEG, CTAB-AuNRs, and AuNRs@MnMEIOs-PEG. The CTAB-AuNRs has two absorption bands at 520 nm (transverse band) and 800 nm (longitudinal band). After conjugating with MnMEIOs, the longitudinal band was blue-shifted from 800 to 788 nm and the color of AuNRs@MnMEIOs-PEG was near red-wine as shown in Figure S1A inset. We speculated that slightly blue-shift of AuNRs@MnMEIOs-PEG may result from incomplete protection in modified process [33,34]. Compare with CTAB-AuNRs, the longitudinal band was evidently blue-shifted and CTAB-AuNRs would aggregate during CTAB removal from the surface of AuNRs (Figure S1B). Photograph in Figure S2A illustrated excellent colloidal stability of AuNRs@MnMEIOs-PEG in PBS even in presence of an external magnet, indicating that AuNRs@MnMEIOs-PEG can be manipulated in the presence of an external magnetic field. Compared with others reports, most Au-SPIO complexes lose their colloidal stability in external magnet [35–37], and severe aggregations would preclude their applications *in vivo*, because their circulation time is very short and they can sometimes cause organ damage result from capillary occlusion [38]. In this study, the high colloidal stability of AuNRs@MnMEIOs-PEG could be attributed to steric stabilization provided by AuNRs and PEG to avoid MnMEIOs interact to each other and resulted in good colloidal stability [39,40]. Stability of AuNRs@MnMEIOs-PEG dispersions to excess electrolytes (PBS) exhibited a similar trend. The images shown in Figure S2B indicate that PEG produces stable dispersions after 6 month of storage. The normalized saturation magnetization of AuNRs@MnMEIOs-PEG at 300 K was 52 emu g^{-1} (Figure S2C). To convert from magnetization per total mass of particles to a basis of per mass of [Fe + Mn], the mass ratio of Au/Fe/Mn was about 3:2:1, as determined by ICP-AES and EDX. The magnetization of approached the value of 104 emu $g^{-1}_{[Fe+Mn]}$, which was similar to magnetization of MnMEIO-PEG ($\approx$105 emu $g^{-1}_{[Fe\ +\ Mn]}$), indicating no significant interference from the AuNRs conjugation. None of the samples showed hysteresis, indicating that both MnMEIO-PEG and AuNRs@MnMEIOs nanoclusters retained superparamagnetic property.

3.2. Evaluation of intracellular distribution of AuNRs@MnMEIOs nanoclusters

To confirm the composition of AuNRs@MnMEIOs nanoclusters, ICP-AES and EDX were performed. The spectrum in Figure S3 confirmed the presence of Fe, Mn, and Au atoms in the nanoclusters. Moreover, confocal laser scanning (CLS) microscopy was used to further investigate the distribution of both AuNRs and MnMEIOs. To do this study, we labeled the fluorescent dye, FITC on the MnMEIOs of AuNRs@MnMEIOs-PEG-Herceptin and applied intense laser to excite plasmon emission of AuNRs and induce the fluorescence [41,42] to examine the intracellular distribution of the AuNPs and MnMEIOs using CLS microscopy. Fig. 2 showed the FITC, AuNRs, fluorescence images and their overlaps for SKBR-3 cells incubated with AuNRs@MnMEIOs-FITC-PEG-Herceptin. The intracellular staining results indicated that the green-fluorescent spots of FITC (located on MnMEIOs, Fig. 2A) and red-fluorescent spots of AuNRs (Fig. 2B) were generally merged and the yellow spots were observed in cytoplasm (Fig. 2C). The line profiles of the fluorescence mapping determined by CLS microscopy (Fig. 2D) evidenced the AuNRs and MnMEIO combined with each other. As shown in

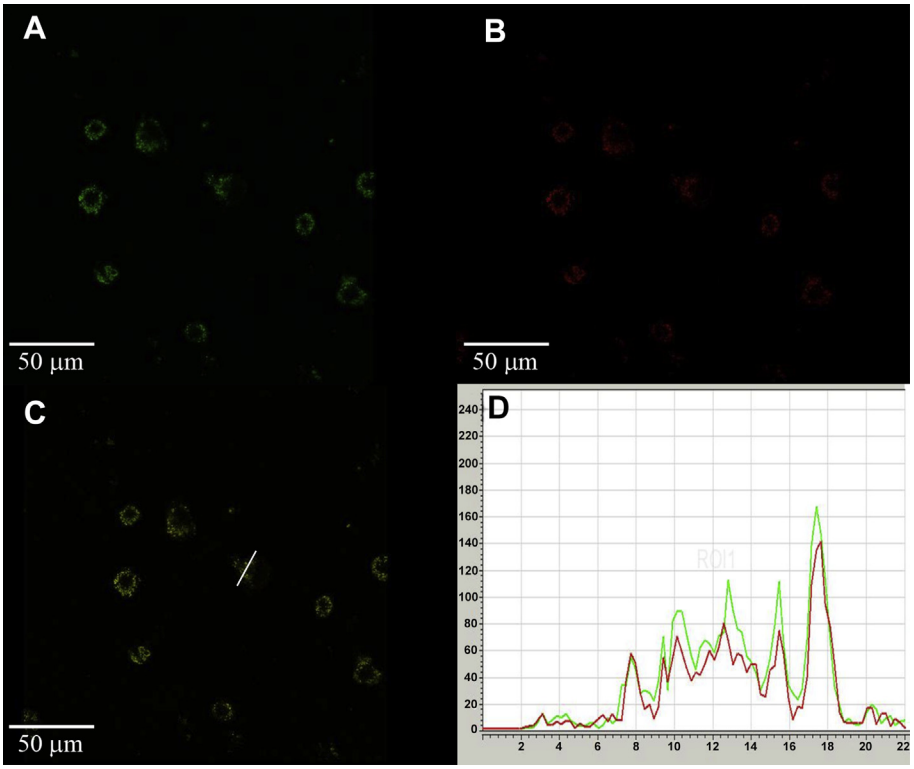

Fig. 2. Fluorescence images of SKBR-3 cell after treated with AuNRs@MnMEIOs-PEG-FITC-Herceptin for 24 h. (A) Green fluorescence showed the location of MnMEIOs; (B) red fluorescence showed the location of AuNRs; (C) physically overlaid image of panels (A) and (B); and (D) A cross sectional compositional (green: MnMEIOs and red: AuNRs) line profile of a single cell under CLS microscopy image. (For interpretation of the references to colour in this figure legend, the reader is referred to the web version of this article.)

Figure S4, we also observed the co-localization for a three-dimensional analysis. These results also indicated that MnMEIOs and AuNRs combined with each other.

3.3. Cytotoxicity assessment

The AuNRs-based nano-platform has been realized and applied in biomedical field, however, AuNRs were reported to induce DNA damage, mitochondria damage and elevate intracellular reactive oxidative species (ROS) due to CTAB [43,44]. Regarding the cytotoxicity of AuNRs@MnMEIOs nanoclusters, the cell viability was assessed as shown in Fig. 3. As expected, MTT cytotoxicity tests revealed no obvious toxic effect of the AuNRs@MnMEIOs-PEG-Herceptin was observed while concentration was below 2 nM (based on AuNRs concentration). It is noteworthy that AuNRs@MnMEIOs nanoclusters evoked excellent biocompatibility and reasonable noncytotoxicity. We speculate that strong AuNRs@MnMEIO binding through MPTES would remove residual CTAB from AuNRs surface, and reduce cytotoxicity of AuNRs to a negligible level.

3.4. Effect of nanocluster shape on cellular uptake

Recent observations in biological systems suggest that particle shape has been considered to play an important role in cellular uptake [45,46]. To our knowledge, it is not clear whether the shape of AuNRs@MnMEIOs nanoclusters have great impact on cellular uptake. To address the effects of shape on cellular uptake, spherical-shaped and rod-shaped AuNRs@MnMEIOs-PEG-Herceptin were chosen in this study (Figure S5). The TEM images (Fig. 4) was conducted to estimate nanoclusters internalization by cells. As shown in Fig. 4, for a single cell, multiple vesicles containing spherical-shaped AuNRs@MnMEIOs-PEG-Herceptin were readily observed (Fig. 4B–F). On the other hand, the TEM image of rod-shaped AuNRs@MnMEIOs-PEG-Herceptin uptake showed no uptake for the same conditions (Fig. 4A). According to visual assessment, the cellular uptake of AuNRs@MnMEIOs-PEG-Herceptin is highly dependent on the shape, in which the results are consistent with cellular uptake of AuNRs [45–47]. Typical Prussian blue staining was performed to demonstrate the nanocluster internalization. As shown in Figure S6A-B, rod-shaped AuNPs@MnMEIOs-PEG-Herceptin internalization were less than that of spherical-shaped AuNRs@MnMEIOs-PEG-Herceptin ones. In addition, Herceptin-modified nanoclusters showed higher uptake in comparison to PEG-coated nanoclusters (Figure S5C-D). The

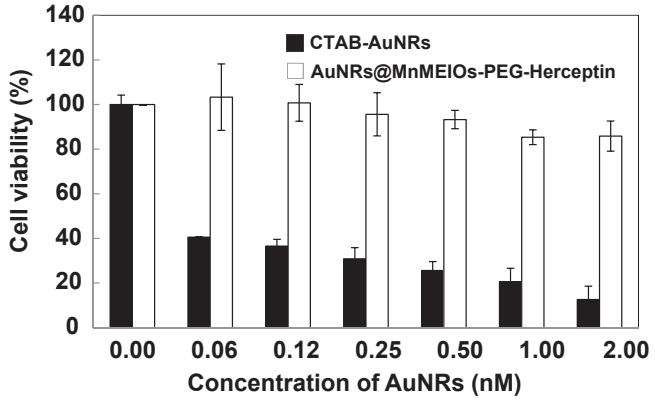

Fig. 3. *In vitro* cytotoxicity of AuNRs@MnMEIOs-PEG-Herceptin and CTAB-AuNRs at different concentrations (62.5 pM–2 nM based on AuNRs) against SKBR-3 cells assessed by MTT assay.

intracellular iron contents for the four types of AuNRs@MnMEIOs nanocluster in SKBR-3 was carried out as shown in Figure S5E. SKBR-3 incubated with spherical-shaped AuNPs@MnMEIOs-PEG-Herceptin resulted in a striking increase in iron contents by a factor of 5 as compared to other three groups. We speculated that the rod-shaped nanoclusters need larger contact area with the cell membrane receptors than the spherical-shaped ones, and the lower amounts of rod-shaped nanoclusters uptake was observed in comparison to the spherical-shaped ones. By taking the overall uptake nanoclusters, spherical-shaped nanoclusters was selected for the following experiments.

3.5. In vitro MR imaging study

To assess the potential use of AuNRs@MnMEIOs nanoclusters as an enhanced MR imaging contrast agent, the T_2 relaxivity value (r_2) of the AuNRs@MnMEIOs-PEG was determined in 20- and 60-MHz relaxometers and compared with that of the MnMEIO-PEG. As shown in Table S2, we summarized the relaxivity values of MnMEIO-PEG, AuNRs@MnMEIOs-PEG and Resovist using 20-MHz and 60-MHz relaxometer. The r_2 relaxivity value of monodispered MnMEIO-PEG was 191.2 ± 2.3 mM^{-1} s^{-1}at 0.5 T. In contrast, MnMEIOs decorated with AuNRs, AuNRs@MnMEIOs-PEG, exhibited a dramatically increased r_2 value of 364.0 ± 2.8 mM^{-1} s^{-1}. Resovist, a clinically approved *T_2-weighted* MR imaging contrast agent, has slightly lower relaxivity value than that of MnMEIO-PEG and significant lower relaxivity values than that of AuNRs@MnMEIOs-PEG [48]. Significant improvement in the r_2 relaxivity value could be attributed to the synergistic magnetic effect of multiple MnMEIOs nanoparticles in one cluster [49,50]. These results suggested that the AuNRs@MnMEIOs-PEG should have a stronger magnetization than that of monodispered MnMEIO and could serve as a more effective contrast agent for MR imaging in clinical diagnosis. *T_2-weighted* images were performed using a 7.0-T MR imaging system. As shown in Figure S7 the negative contrast enhancements were 55.7 ± 2.4%, 32.6 ± 2.7%, 30.8 ± 3.2%, 12.7 ± 1.9%, and 6.2 ± 1.2% by comparing their results to that of MnMEIO-PEG. AuNRs@MnMEIOs-PEG exhibited better negative contrast enhancements than MnMEIO-PEG at different concentrations (12, 25, 50, 100, and 200 μM).

To illustrate the utility of AuNRs@MnMEIOs-PEG-Herceptin for biomedical imaging, we also evaluated cellular uptake of AuNRs@MnMEIOs-PEG-Herceptin in two different cancer cells (Colo-205 and SKBR-3). As shown in Fig. 5, *T_2-weighted* MR images of Colo-205 cells treated with AuNRs@MnMEIOs-PEG-Herceptin and SKBR-3 cells treated with AuNRs@MnMEIOs-PEG exhibited minimal contrast enhancement. The MR images of AuNRs@MnMEIOs-PEG-Herceptin treated SKBR-3 cells (over-express HER-2) showed much more (negative) contrast enhancements (−37.2 ± 3.4%, −49.1 ± 4.5%, −66.1 ± 2.7%, −84.7 ± 5.1%, and −90.0 ± 4.9% along with increasing contrast agent concentration). Different contrast enhancements between SKBR-3 and Colo-205 is most likely attributed to ligand-receptor-mediated internalization of AuNRs@MnMEIOs-PEG-Herceptin by targeted cells [51].

3.6. In vivo MR imaging study

Furthermore, *in vivo T_2-weighted* MR images were observed on nude mice bearing subcutaneous xenografts of SKBR-3 and Colo-205 tumor before and after intravenously injection of AuNRs@MnMEIOs-PEG-Herceptin (10 mg kg^{-1}). As shown in Fig. 6, it is clear that high negative contrast enhancement observed for SKBR-3 tumor (−70.4 ± 7.2%) indicated more accumulation of contrast agents, and moderate or slight negative contrast

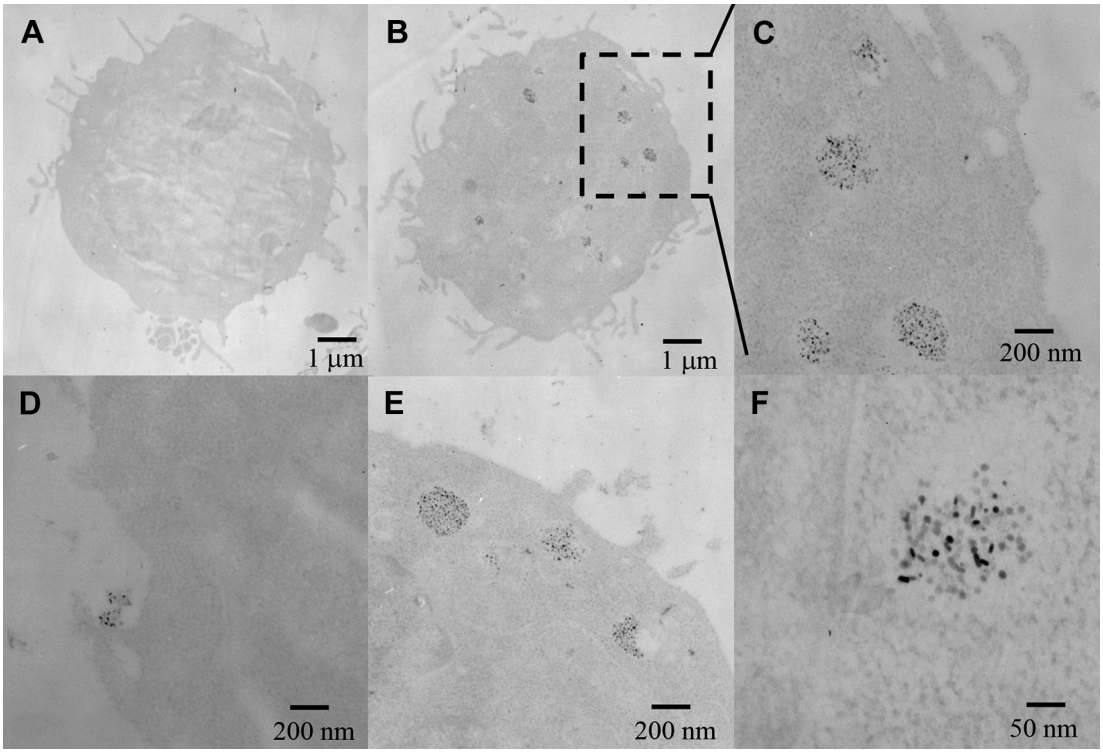

Fig. 4. TEM images of SKBR-3 cells incubated with (A) rod-shaped and (B) spherical-shaped AuNRs@MnMEIOs-PEG-Herceptin for 4 h (C), (D), (E), (F) represent enlarged views of SKBR-3 cells incubated with spherical-shaped AuNRs@MnMEIOs-PEG-Herceptin nanoclusters.

enhancement observed for Colo-205 tumor (−7.5 ± 1.4%). By comparing these results, MR images at 24 h post injection showed significant negative contrast enhancement in SKBR-3 tumor.

In addition, the systematic toxicity of the established AuNRs@MnMEIOs-PEG-Herceptin nanoclusters was examined *in vivo* in our experiment. Histological examinations of major organs indicated no evident tissue damage was observed in these major organs (Figure S8).

3.7. Targeted photothermal tumor treatment

AuNRs are excellent photothermal agents due to their strong absorption and high light-to-thermal conversion efficiency which is about five orders of magnitude higher than that of fluorescent dye [52]. To demonstrate the photothermal conversion effect, AuNRs@MnMEIOs nanoclusters were exposed under the 808 nm laser radiation, which is close to the longitudinal band of AuNRs@MnMEIOs nanoclusters, and the temperature was measured. As shown in Figure S9 a remarkable increase temperature more than 30 °C was observed at the aqueous solution containing 1 nM of AuNRs under 5 W cm^{-2} and 808 nm laser irradiation for 10 min. As previous reports, after laser irradiation, the longitudinal band of AuNRs markedly decrease even if grafted macromolecules on the AuNR surfaces (Figure S10) [33,53]. The blue shift of absorption band would be attributed to the aggregation of the AuNRs. Indeed, to evaluate the aggregate formation of the AuNRs@MnMEIOs-PEG, we measured the absorption spectra of the AuNRs@MnMEIOs-PEG after NIR laser irradiation and found AuNRs@MnMEIOs-PEG showed negligible loss in their longitudinal band after laser irradiation for 10 min (Figure S10). It is likely that

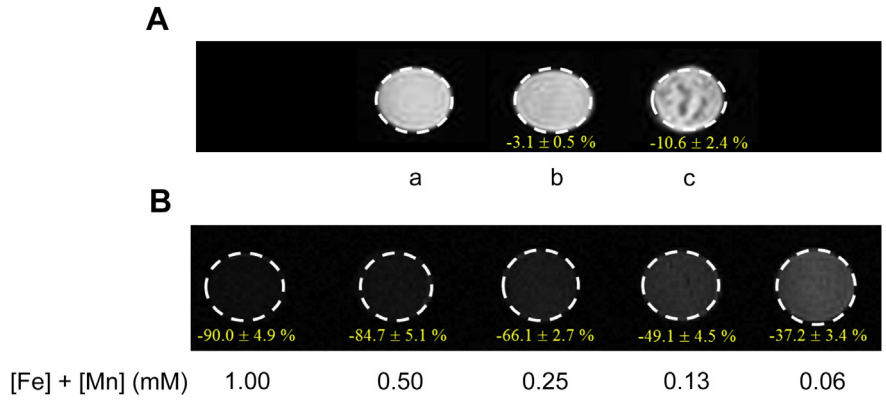

Fig. 5. A) Top: *in vitro* T_2*-weighted* MR images of a) untreated SKBR-3 cells, b) SKBR-3 treated with AuNRs@MnMEIOs-PEG and c) Colo-205 treated with AuNRs@MnMEIOs-PEG-Herceptin; B) bottom: *in vitro* T_2*-weighted* MR images of SKBR-3 cells treated with AuNRs@MnMEIOs-PEG-Herceptin nanoclusters at different concentrations. All of signal enhancements were compared with (a).

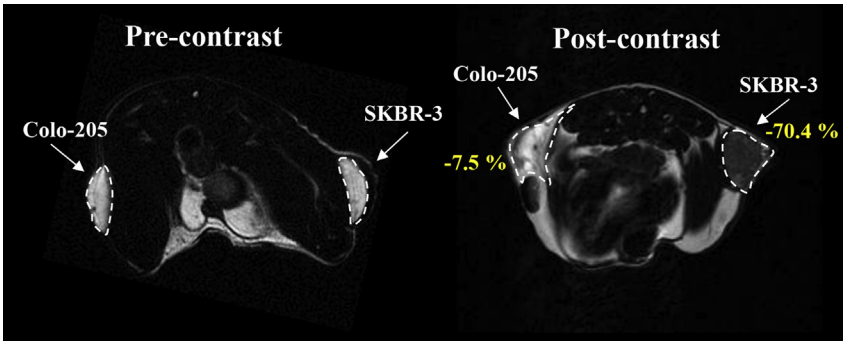

Fig. 6. *In vivo T_2-weighted* MR images of AuNRs@MnMEIOs-PEG-Herceptin accumulating in tumors bearing mice.

the AuNRs@MnMEIOs-PEG nanoclusters have superb thermal stability so that the AuNRs@MnMEIOs-PEG nanoclusters could be particularly suited to long term thermal therapy. Recent studies have reported the use of confined and thermally-stable materials such as carbon and silica to trap AuNRs, thereby enabling highly thermal stability [54]. We speculated that such limitations could be overcome by embedding AuNRs with MnMEIOs nanoparticles to protect from aggregation.

Effective internalization provides an opportunity to apply selective destruction of cancer cells upon irradiation by 808 nm NIR laser. To demonstrate the photothermal effect *in vitro*, the SKBR-3 cells were treated with AuNRs@MnMEIOs-PEG-Herceptin and laser irradiated at varying intensities. The localized cell photothermal effect was further investigated as shown in Fig. 7.With the treatment of AuNRs@MnMEIOs-PEG-Herceptin, a clear demarcation line between dead (red) and live cell (green) regions can be observed in presence of laser exposure at 5 W cm^{-2} for 10 min. It is demonstrated that AuNRs@MnMEIOs-PEG-Herceptin could kill cells only through the photothermal effect induced by NIR laser irradiation, while neither the AuNRs@MnMEIOs-PEG-Herceptin itself nor the laser irradiation alone can kill SKBR-3 cells.

3.8. Photothermal therapy in vivo

For an *in vivo* photothermal therapy, nude mice subcutaneously transplanted with SKBR-3 cells on their right thighs were used. After the mouse was injected with AuNRs@MnMEIOs-PEG-Herceptin for 24 h, tumor of each mouse in the treatment group was exposed to an 808 nm laser at a power density of 5 W cm^{-2} for 10 min and recorded with an IR camera in real time (Figure S11). As shown in Fig. 8A, after mouse tumors were AuNRs@MnMEIOs-PEG-Herceptin, followed by irradiation with the laser, the tumor growth was significantly suppressed. In addition, a charring spot appears on the tumor site. In this irradiation group, one mouse tumor was completely eliminated on day 5 of irradiation. In contrast, the tumors in the control animals injected with solely PBS or AuNRs@MnMEIOs-PEG-Herceptin without irradiation or solely laser grow markedly over time (Fig. 8B). Importantly, mice in the four control groups had an average life span of 14–26 days, while mice in the treated group (AuNRs@MnMEIOs-PEG-Herceptin + laser) were tumor-free after treatment and survived over 40 days (Fig. 8C). Our results suggest that AuNRs@MnMEIOs-PEG-Herceptin is a powerful agent for *in vivo* photothermal therapy of cancer.

4. Conclusions

We have reported the successful strategy toward the ultimate goal of cancer diagnosis and therapy. This established AuNRs@MnMEIOs nanoclusters features high stability, monodispersity with an average hydrodynamic diameter of approximately 60 nm, superparamagnetic property, low cytotoxicity, and highly

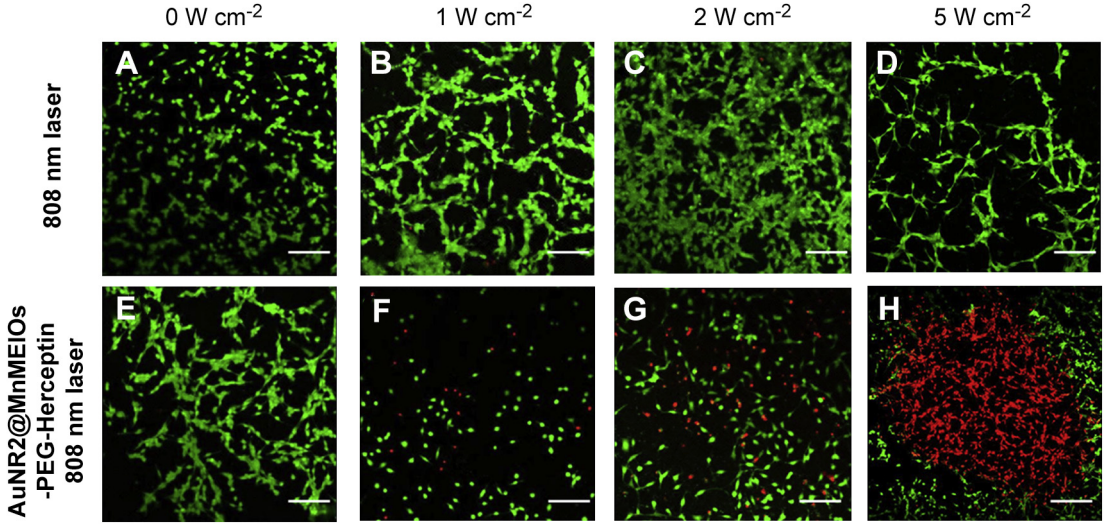

Fig. 7. Cells incubated with AuNRs@MnMEIOs-PEG-Herceptin and then irradiated by an 808 nm laser for 10 min at different power densities. The first row shows laser alone while the second row AuNRs@MnMEIOs-PEG-Herceptin and 808 nm laser treatment. Each column shows cells treated at specific laser intensity: 0 W cm^{-2} ((A), (F)), 1 W cm^{-2} ((B), (G)), 2 W cm^{-2} ((C), (H)), and 5 W cm^{-2} ((d), (i)) Viable cells appear green from calcein AM staining while red areas of PI fluorescence are cells destroyed by photothermal irradiation. Scale bar 200 μm for all images. (For interpretation of the references to colour in this figure legend, the reader is referred to the web version of this article.)

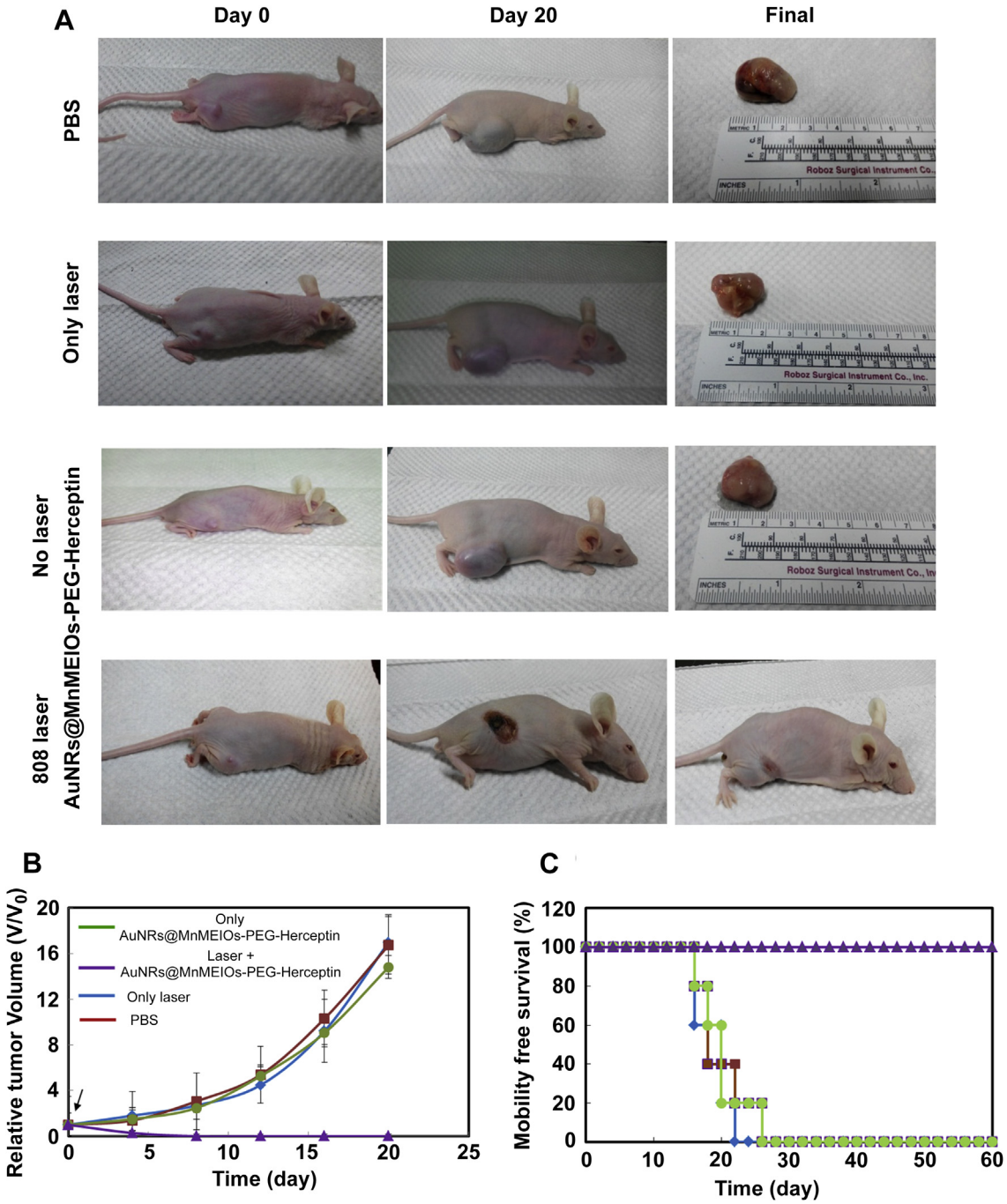

Fig. 8. *In vivo* photothermal therapy. (A) Representative photos of tumors with and without laser irradiation or AuNRs@MnMEIOs-PEG-Herceptin treatment; (B) Tumor growth curves in different groups of mice after treatment ($n = 5$) (where the arrows labeled). The tumor volumes were normalized to their initial sizes. Error bars were based on SD; (C) Survival curves of mice bearing SKBR-3 tumor after various treatments indicated.

efficient photothermal effect. The AuNRs@MnMEIOs nanoclusters showed transversal relaxivity at least about 2 times higher than commercial contrast agents. On the other hand, the spherical-shaped nanoclusters were easily engulfed by cells and demonstrated that the fabricated AuNRs@MnMEIOs nanocluster can kill cancer cells effectively with exposure to NIR laser. In addition, these dual functional nanoclusters have a great potential for *in vitro* and *in vivo* MR imaging diagnosis and photothermal tumor therapy. Since the AuNRs of these nanoclusters can provide heat while NIR laser treatment, this technique will provide functional options for achieving an advanced controlled-release system using AuNRs for drug therapy responding to NIR stimuli.

Acknowledgments

This work was supported by grants NSC 102-227-M-009-004-MY3 and NSC 101-2923-M-009-002-MY3 from the National Science Council of Taiwan and MOHW 103-TD-B-111-05 from Ministry of Health and Welfare. This research was also particularly supported by “Aim for the Top University Plan” of the National Chiao Tung University and Ministry of Education. The authors thank to Ms. C.-Y. Chien of Precious Instrument Center (National Taiwan University) for the assistance in TEM experiment and Ms. H. −F. Chen for the assistance in MRI experiment.

Appendix A. Supplementary data

Supplementary data related to this article can be found at http://dx.doi.org/10.1016/j.biomaterials.2014.02.026.

References

[1] Katz E, Willner I. Integrated nanoparticle-biomolecule hybrid systems: synthesis, properties, and applications. Angew Chem Int Ed Engl 2004;43:6042–108.
[2] Ferrari M. Cancer nanotechnology: opportunities and challenges. Nat Rev Cancer 2005;5:161–71.
[3] Lal S, Clare SE, Halas NJ. Nanoshell-enabled photothermal cancer therapy: impending clinical impact. Acc Chem Res 2008;41:1842–51.
[4] Bao G, Mitragotri S, Tong S. Multifunctional nanoparticles for drug delivery and molecular imaging. Annu Rev Biomed Eng 2013;15:253–82.
[5] Gao J, Gu H, Xu B. Multifunctional magnetic nanoparticles: design, synthesis, and biomedical applications. Acc Chem Res 2009;42:1097–107.
[6] Lu W, Singh AK, Khan SA, Senapati D, Yu H, Ray PC. Gold nano-popcorn based targeted diagonosis, nanotherapy treatment and in-situ monitoring of photothermal therapy response of prostate cancer cells using surface enhanced raman spectroscopy. J Am Chem Soc 2010;132:18103–14.
[7] Koo HM, Huh S, Sun IC, Yuk SH, Choi K, Kim K, et al. *In vivo* targeted delivery of nanoparticles for theranosis. Acc Chem Res 2011;44:1018–28.
[8] Xie J, Liu G, Eden HS, Ai H, Chen X. Surface-engineered magnetic nanoparticle platforms for cancer imaging and therapy. Acc Chem Res 2011;44:883–92.
[9] Fan Z, Shelton M, Singh AK, Senapati D, Khan SAP, Ra C. Multifunctional plasmonic shell magnetic core nanoparticles for targeted diagnostics, isolation, and photothermal destruction of tumor cells. ACS Nano 2012;6:1065–73.
[10] Bao J, Chen W, Liu T, Zhu Y, Jin P, Wang L, et al. Bifunctional Au-Fe_3O_4 nanoparticles for protein separation. ACS Nano 2007;1:293–8.
[11] Xu C, Xie J, Ho D, Wang C, Kohler NE, Walsh G, et al. Au-Fe_3O_4 dumbbell nanoparticles as dual-functional probes. Angew Chem Int Ed 2008;47:173–6.
[12] Lyon JL, Fleming DA, Stone MB, Schiffer PM, Williams E. Synthesis of Fe oxide core/Au shell nanoparticles by iterative hydroxylamine seeding. Nano Lett 2004;4:719–23.
[13] Xu Z, Hou Y, Sun S. Magnetic core/shell Fe_3O_4/Au and Fe_3O_4/Au/Ag nanoparticles with tunable plasmonic properties. J Am Chem Soc 2007;129:8698–9.
[14] Wang L, Bai J, Li Y, Huang Y. Multifunctional nanoparticles displaying magnetization and near-IR absorption. Angew Chem Int Ed 2008;47:2439–42.
[15] Ma LL, Feldman MD, Tam JM, Paranjape AS, Cheruku KK, Larson TA, et al. Small multifunctional nanoclusters (nanoroses) for targeted cellular imaging and therapy. ACS Nano 2009;3:2686–96.
[16] Hirsch LR, Stafford RJ, Bankson JA, Sershen SR, Rivera B, Price RE, et al. Nanoshell-mediated near-infrared thermal therapy of tumors under magnetic resonance guidance. Proc Natl Acad Sci 2003;100:13549–54.
[17] Chen J, Wang D, Xi J, Au L, Siekkinen A, Warsen A, et al. Immuno gold nanocages with tailored optical properties for targeted photothermal destruction of cancer cells. Nano Lett 2007;7:1318–22.
[18] Madsen SJ, Baek SK, Makkouk AR, Krasieva T, Hirschberg H. Macrophages as cell-based delivery systems for nanoshells in photothermal therapy. Ann Biomed Eng 2012;40:507–15.
[19] Larson TA, Bankson J, Aaron J, Sokolov K. Hybrid plasmonic magnetic nanoparticles as molecular specific agents for MRI/optical imaging and photothermal therapy of cancer cells. Nanotechnology 2007;18:325101–8.
[20] Elsherbini AA, Saber M, Aggag M, El-Shahawy A, Shokier HA. Laser and radiofrequency-induced hyperthermia treatment via gold-coated magnetic nanocomposites. Int J Nanomedicine 2011;6:2155–65.
[21] Narayanan S, Sathy BN, Mony U, Koyakutty M, Nair SV, Menon D. Biocompatible magnetite/gold nanohybrid contrast agents via green chemistry for MRI and CT bioimaging. ACS Appl Mater Interfaces 2012;4:251–60.
[22] Liu H, Chen D, Li L, Liu T, Tan L, Wu X, et al. Multifunctional gold nanoshells on silica nanorattles: a platform for the combination of photothermal therapy and chemotherapy with low systemic toxicity. Angew Chem Int Ed 2011;50:891–5.
[23] Melancon MP, Lu W, Zhong M, Zhou M, Liang G, Elliott AM, et al. Targeted multifunctional gold-based nanoshells for magnetic resonance-guided laser ablation of head and neck cancer. Biomaterials 2011;32:7600–8.
[24] Bardhan R, Lal S, Joshi A, Halas NJ. Theranostic nanoshells: from probe design to imaging and treatment of cancer. Acc Chem Res 2011;44:936–46.
[25] Sun S, Zeng H, Robinson DB, Raoux S, Rice PM, Wang SX, et al. Monodisperse MFe_2O_4 (M = Fe, Co, Mn) nanoparticles. J Am Chem Soc 2004;126:273–9.
[26] Levin CS, Hofmann C, Ali TA, Kelly AT, Morosan E, Nordlander P, et al. Magnetic plasmonic coreshell nanoparticles. ACS Nano 2009;3:13791388.
[27] Si S, Leduc C, Delville MH, Lounis B. Short gold nanorod growth revisited: the critical role of the bromide counterion. Chemphyschem. 2011;13:193–202.
[28] Ye X, Zheng C, Chen J, Gao Y, Murray CB. Using binary surfactant mixtures to simultaneously improve the dimensional tunability and monodispersity in the seeded growth of gold nanorods. Nano Lett 2013;13:765–71.
[29] Orendorff CJ, Murphy CJ. Quantitation of metal content in the silver-assisted growth of gold nanorods. J Phys Chem B 2006;110:3990–4.
[30] Wu SC, Lin KL, Wang TP, Tzou SC, Singh G, Chen MH, et al. Imaging specificity of MR-optical imaging agents following the masking of surface charge by poly(ethylene glycol). Biomaterials 2013;34:4118–27.
[31] Lipka J, Semmler-Behnke M, Sperling RA, Wenk A, Takenaka S, Schleh C, et al. Biodistribution of PEG-modified gold nanoparticles following intratracheal instillation and intravenous injection. Biomaterials 2010;31:6574–81.
[32] Niidome T, Yamagata M, Okamoto Y, Akiyama Y, Takahashi H, Kawano T, et al. PEG-modified gold nanorods with a stealth character for in vivo applications. J Control Release 2006;114:343–7.
[33] Yamashita S, Fukushima H, Niidome Y, Mori T, Katayama Y, Niidome T. Controlled-release system mediated by a retro Diels-Alder reaction induced by the photothermal effect of gold nanorods. Langmuir 2011;27:14621–6.
[34] Kawamura G, Yang Y, Nogami M. Facile assembling of gold nanorods with large aspect ratio and their surface-enhanced Raman scattering properties. Appl Phys Lett 2007;90:261908–10.
[35] Wang DW, Zhu XM, Lee SF, Chan HM, Li HW, Kong SK, et al. Folate-conjugated Fe_3O_4@SiO_2@gold nanorods@mesoporous SiO_2 hybrid nanomaterial: a theranostic agent for magnetic resonance imaging and photothermal therapy. J Mater Chem B 2013;1:2934–42.
[36] Ma M, Chen H, Chen Y, Wang X, Chen F, Cui X, et al. Au capped magnetic core/mesoporous silica shell nanoparticles for combined photothermo-/chemotherapy and multimodal imaging. Biomaterials 2012;33:989–98.
[37] Wang C, Chen J, Talavage T, Irudayaraj J. Gold nanorod/Fe_3O_4 nanoparticle "nano-pearl-necklaces" for simultaneous targeting, dual-mode imaging, and photothermal ablation of cancer cells. Angew Chem Int Ed 2009;48:27592763.
[38] Kievit FM, Zhang M. Surface engineering of iron oxide nanoparticles for targeted cancer therapy. Acc Chem Res 2011;44:853–62.
[39] Liong M, Lu J, Kovochich M, Xia T, Ruehm SG, Nel AE, et al. Multifunctional inorganic nanoparticles for imaging, targeting, and drug delivery. ACS Nano 2008;2:889–96.
[40] Lee N, Choi Y, Lee Y, Park M, Moon WK, Choi SH, et al. Water-dispersible ferrimagnetic iron oxide nanocubes with extremely high r_2 relaxivity for highly sensitive *in vivo* MRI of tumors. Nano Lett 2012;12:3127–31.
[41] Goldys EM, Sobhan MA. Fluorescence of colloidal gold nanoparticles is controlled by the surface adsorbate. Adv Funct Mater 2012;22:1906–13.
[42] Eustis S, El-Sayed M. Aspect ratio dependence of the enhanced fluorescence intensity of gold nanorods: experimental and simulation study. J Phys Chem B 2005;109:16350–6.
[43] Zhao F, Zhao Y, Liu Y, Chang X, Chen C, Zhao Y. Cellular uptake, intracellular trafficking, and cytotoxicity of nanomaterials. Small 2011;7:1322–37.
[44] Rayavarapu RG, Petersen W, Hartsuiker L, Chin P, Janssen H, van Leeuwen FW, et al. *In vitro* toxicity studies of polymer-coated gold nanorods. Nanotechnology 2010;21:145101–10.
[45] Chithrani BD, Chan WC. Elucidating the mechanism of cellular uptake and removal of protein-coated gold nanoparticles of different sizes and shapes. Nano Lett 2007;7:1542–50.
[46] Chithrani BD, Ghazani AA, Chan WC. Determining the size and shape dependence of gold nanoparticle uptake into mammalian cells. Nano Lett 2006;4:662–8.
[47] Qiu Y, Liu Y, Wang L, Xu L, Bai R, Ji Y, et al. Surface chemistry and aspect ratio mediated cellular uptake of Au nanorods. Biomaterials 2010;31:7606–19.
[48] Qin J, Laurent S, Jo YS, Roch A, Mikhaylova M, Bhujwalla ZM, et al. A high-performance magnetic resonance imaging T_2 contrast agent. Adv Mater 2007;19:1874–8.
[49] Yoon TJ, Lee H, Shao H, Hilderbrand SA, Weissleder R. Multicore assemblies potentiate magnetic properties of biomagnetic nanoparticles. Adv Mater 2011;23:4793–7.
[50] Lee JE, Lee N, Kim H, Kim J, Choi SH, Kim JH, et al. Uniform mesoporous dye-doped silica nanoparticles decorated with multiple magnetite nanocrystals for simultaneous enhanced magnetic resonance imaging, fluorescence imaging, and drug delivery. J Am Chem Soc 2010;132:552–7.
[51] Meier R, Henning TD, Boddington S, Tavri S, Arora S, Piontek G, et al. Breast cancers: MR imaging of folate-receptor expression with the folate-specific nanoparticle P1133. Radiology 2010;255:527–35.
[52] Yi DK, Sun IC, Ryu JH, Koo H, Park CW, Youn IC, et al. Matrix metalloproteinase sensitive gold nanorod for simultaneous bioimaging and photothermal therapy of cancer. Bioconjug Chem 2010;21:2173–7.
[53] Cheng L, Yang K, Li Y, Zeng X, Shao MS, Lee T, et al. Multifunctional nanoparticles for upconversion luminescence/MR multimodal imaging and magnetically targeted photothermal therapy. Biomaterials 2012;33:2215–22.
[54] Yang HW, Liu HL, Li ML, Hsi IW, Fan CT, Huang CY, et al. Magnetic gold-nanorod/PNIPAAmMA nanoparticles for dual magnetic resonance and photoacoustic imaging and targeted photothermal therapy. Biomaterials 2013;34:5651–60.